Journal of *Marine Science and Engineering*

MDPI

Article

Sequential Evolution of Residual Liquefaction in a Silty Seabed: Effect of Wave-Loading History

Changfei Li [1,2], Yifa Wang [3], Jiahao Yu [1,2], Wengang Qi [1,2] and Fuping Gao [1,2,*]

1 Institute of Mechanics, Chinese Academy of Sciences, Beijing 100190, China; lichangfei@imech.ac.cn (C.L.); yujiahao@imech.ac.cn (J.Y.); qiwengang@imech.ac.cn (W.Q.)
2 School of Engineering Science, University of Chinese Academy of Sciences, Beijing 100049, China
3 Department of Infrastructure Engineering, Faculty of Engineering and Information Technology, The University of Melbourne, Melbourne, VIC 3010, Australia; yifa.wang@unimelb.edu.au
* Correspondence: fpgao@imech.ac.cn

Abstract: Multiple liquefaction events may occur if a seabed is subjected to repeated but intermittent wave loadings. This study aimed to investigate the influence of the wave-loading history on the evolution of residual liquefaction in a silty seabed through a series of wave flume tests. The flume observations reveal that the preceding wave-loading history results in the densification of the silt bed and a noticeable settlement of the mudline. Meanwhile, the ultimate liquefaction depth, maximum amplitude of interfacial waves, and mudline settlement decrease due to prior wave actions. Both the maximum residual pore pressure ratio and the amplification ratio of transient pore pressure exhibit a declining trend with an increasing number of wave exposures, indicating that the liquefaction resistance of the soil is obviously enhanced. Throughout the continuous liquefaction stage, the residual pore pressure in liquefied soil regions maintains its maximum value. In contrast, the pore pressure in the un-liquefied soil layer experiences slight dissipation after reaching its peak during wave activity. Moreover, the reshaped topography of the silt bed following liquefaction-densification cycles may serve as an indicator of prior liquefaction events, transforming from mud volcanoes into ripples as the liquefaction depth decreases.

Keywords: residual liquefaction; excess pore pressure; wave-loading history; silty seabed; flume observation

check for updates

Citation: Li, C.; Wang, Y.; Yu, J.; Qi, W.; Gao, F. Sequential Evolution of Residual Liquefaction in a Silty Seabed: Effect of Wave-Loading History. *J. Mar. Sci. Eng.* **2024**, *12*, 750. https://doi.org/10.3390/jmse12050750

Academic Editor: Angelo Rubino

Received: 27 December 2023
Revised: 26 April 2024
Accepted: 26 April 2024
Published: 30 April 2024

1. Introduction

Severe wave loading can cause liquefaction in a seabed, leading to the potential instability or failure of offshore structures [1–7]. The evaluation of wave-induced seabed liquefaction is a critical concern in the design of offshore foundations.

Two primary mechanisms of wave-induced liquefaction have been identified, i.e., instantaneous liquefaction and residual liquefaction [8,9]. Instantaneous liquefaction, also known as momentary liquefaction, arises from transient pore pressure induced by upward seepage forces in the upper seabed layer during wave troughs [10,11]. Various theoretical models regarding wave-induced transient pore pressure have been proposed, based on various assumptions about the soil skeleton and pore fluid characteristics in a porous seabed [12–18]. Meanwhile, criteria for instantaneous liquefaction have been established to assess the depth of instantaneously liquefied soil [8,19–21].

In contrast, residual liquefaction occurs when the effective stress of the soil reduces to zero due to residual pore pressure buildup [10,22]. The physical modeling of wave-induced pore pressure buildup and the associated residual liquefaction has been achieved through flume observations [23–25] and centrifuge tests [26,27]. Notably, Sumer et al. [24] successfully replicated the complete sequence of silt behavior under progressive waves in flume experiments, including pore pressure buildup, liquefaction, compaction, pore pressure dissipation, and ripple formation. Li et al. [25] provided insights into the spatiotemporal evolution of both residual and transient pore pressure in a silt bed subjected to progressive waves, identifying three distinct stages of residual liquefaction. These stages include quasi-elastic behavior, an intensive buildup of residual pore pressure, and continuous liquefaction, with a particular focus on transient pore pressure amplification. The amplification ratio of transient pore pressure during the continuous liquefaction stage was found to be one order of magnitude larger than that during the quasi-elastic stage. Sassa and Sekiguchi [26], through centrifuge modeling, reported the progressive nature of soil liquefaction, with the liquefaction front advancing downward. Critical cyclic stress ratios below which liquefaction does not occur have been identified for a given wave-loading regime. Furthermore, advances in understanding wave-induced residual liquefaction have been made through theoretical analyses [28–31] and numerical simulations [5,22,32–35].

In offshore environments, the seabed is frequently subjected to repeated wave loadings, emphasizing the significance of considering the wave-loading history in the evaluation of soil liquefaction. Once soil undergoes liquefaction, its response to subsequent waves may be altered. For instance, liquefaction leads to significant densification during the dissipation of excess pore pressure [24,26,27]. Sumer et al. [2] carried out supplementary flume experiments to investigate the effect of wave exposure history, revealing a substantial reduction in the maximum residual pore pressure during subsequent exposures. Centrifuge tests by Sassa and Sekiguchi [26] demonstrated a shallower re-liquefaction depth of the sand bed with each successive wave-reloading stage. Sui et al. [36] reported experimental results on wave-induced silt liquefaction under multiple exposures, highlighting that the initial strongest wave in a sequence "secures" the onset of liquefaction, independent of prior exposures. However, the existing studies on the wave-loading history effect have primarily focused on the residual pore pressure and liquefied soil depth, neglecting the associated transient pore pressure. Additionally, the influence of the wave-loading history on the post-liquefaction bed topography remains poorly described.

This paper aimed to explore the effect of the wave-loading history on the evolution of residual liquefaction in a silty seabed. A series of wave flume experiments were conducted to comprehensively examine the multi-mechanical processes of the silt bed under repeated but alternating progressive waves, including pore pressure buildup and dissipation, liquefaction occurrence, transient pore pressure amplification, and bed topography formation.

2. Experimental Methodology

Building upon the earlier work of Li et al. [25], which mainly focused on the silt responses under a single wave-loading series, this study conducted flume observations to examine the effect of the wave-loading history on residual liquefaction. Specifically, the single test series reported by Li et al. [25] is denoted as Test 1 in this paper. Thus, the experimental methodology adopted in this study closely aligns with that detailed in Li et al.'s study [25]. This section provides a brief overview of the flume setup, bed preparation, and testing procedure.

2.1. Flume Set-Up

A series of flume tests were conducted in a large wave flume of 52.0 m (length) $\times$ 1.0 m (width) $\times$ 1.5 m (depth) (see Figure 1) at the Institute of Mechanics, the Chinese Academy of Sciences. A piston-type wave generator installed at the inlet of the flume was employed to generate steady progressive waves, given the wave period as well as the wave height. The free surface elevation of waves and wave-induced pore pressures at various soil depths were simultaneously monitored with four wave gauges (WGs) and seven miniature pore pressure transducers (PPTs), respectively. A detailed introduction to the flume set-up can be referenced in Li et al.'s study [25].

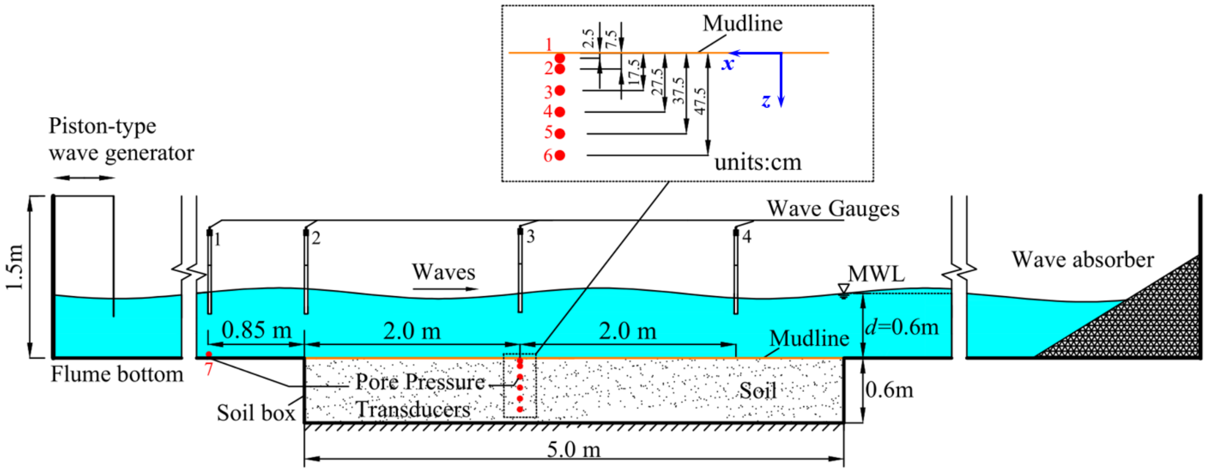

Figure 1. Flume set-up for wave-induced liquefaction of a silt bed (note: the buried depths of PPTs correspond to Test 1; d is the water depth).

2.2. Silt Bed Preparation

The silt bed was carefully prepared using the sand-raining technique, whereby dry silt particles in a reciprocating trolley were rained into the water within the soil box. This process ensured the creation of a homogeneous and quasi-fully saturated silt bed. Prior to subjecting the bed to wave loadings, the surface of the silt bed was leveled with a scraper.

Figure 2a,b shows the typical topography of silt grains captured by SEM and the grain size distribution curve, respectively. The main physical properties of the silt are summarized in Table 1. The specific gravity (G_s), water content (w), void ratio (e), and relative density (D_r) were obtained as outlined in Li et al. [25]. Chapius [37] proposed a simplified equation to evaluate the coefficient of permeability (k_s) of soil, which can be expressed as:

$$k_s(\text{cm/s}) \approx 2.46\left(\frac{e^3}{1+e}d_{10}^2\right)^{0.78} \quad (1)$$

where d_{10} is the effective grain size and is measured in mm. Equation (1) indicates that k_s exhibits a substantial increase with increasing e. The measured plasticity index I_p was approximately 9.0. It has been identified that the shear behavior of silt transitions from sand-like to clay-like material as I_p increases from 2 to 9 [38]. Through triaxial tests, the cohesion (c) and the angle of internal friction (φ) of the silt were obtained. In this study, four repeated wave-loading series were applied to the prepared silt bed (see Section 2.3). Due to the soil densification mechanism, as further discussed in Section 3.1, the soil properties (including e, D_r, k_s, and γ') were altered by the preceding wave-loading history, as listed in Table 1. The plasticity index (I_p), cohesion (c), and angle of internal friction (φ) of the silt may also be related to the soil density. However, to streamline testing procedures, only the initial values of I_p, c, and φ before raining the silt into the soil box were measured. It should be noted that all the various soil properties (including e, D_r, k_s, and γ') in Table 1 correspond to the pre-test condition, i.e., before subjecting the silt bed to progressive waves in each test series.

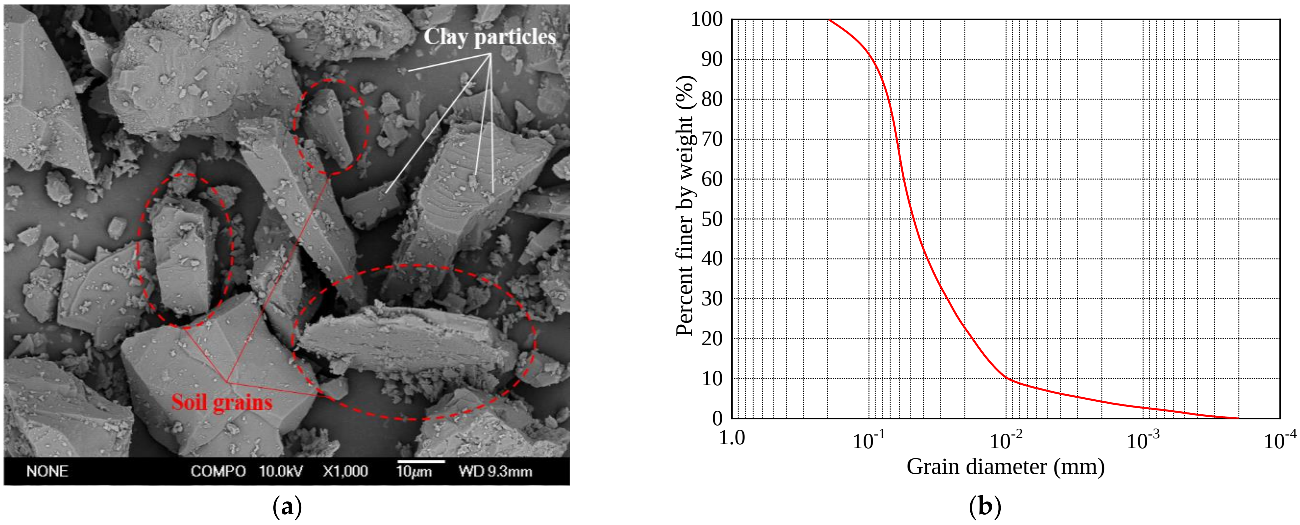

Figure 2. Soil grains of the test silt: (**a**) typical SEM image; (**b**) grain size distribution.

Table 1. Silt properties corresponding to each test series.

Soil Property	Symbol	Value	Test Series			
			Test 1	Test 2	Test 3	Test 4
Mean grain size	d_{50} (mm)	0.047				
Effective grain size	d_{10} (mm)	0.009				
Specific gravity of grains	G_s	2.65				
Maximum void ratio	e_{max}	1.14				
Minimum void ratio	e_{min}	0.23				
Void ratio	e	-	0.54	0.49	0.45	0.43
Relative density	D_r	-	0.66	0.71	0.76	0.78
Coefficient of permeability	k_s ($\times 10^{-6}$ m/s)	-	3.34	2.60	2.12	1.78
Submerged unit weight of soil	γ' (kN/m^3)	-	10.71	11.07	11.38	11.54
Plasticity index	I_p (%)	9.0				
Cohesion	c (kPa)	6.35				
Friction angle	φ (°)	27.4				

2.3. Test Procedures

The following test procedures were adopted:

(1) All PPTs, whose argil covers were first de-aired, were calibrated and then installed at varying soil depths with the support of fixing racks within the soil box (Figure 1). The WGs were also calibrated before their installations.

(2) The silt bed was prepared by employing the sand-raining technique. The bed surface was then leveled off smoothly using a scraper.

(3) The flume was gradually filled with water to a given depth (d = 0.6 m), which was maintained constant throughout all four test series.

(4) The piston-type wave generator was then activated, and the progressive regular waves were generated. Meanwhile, the signals of the WGs and PPTs were simultaneously logged by the multichannel synchronous sampling system with a sampling frequency of 25 Hz. The wave height (H) and the wave period (T) of the waves were adopted as H = 8.0 cm and T = 1.5 s, respectively.

(5) The wave generator was deactivated after a loading duration of 3600 s, while the data acquisition system continued logging until the residual pore pressure fully dissipated.

(6) After a hydrostatic duration exceeding 24 h (1 day), the suspended silt particles in the wave flume underwent complete settlement. Subsequently, the settlement of the mudline (s) was observed through the glass sidewall of the flume, accompanied by a snapshot capturing the surface topography of the silt bed.

(7) The testing procedures outlined in steps (4)~(6) were repeated four times, constituting four test series (Tests 1~4; see Table 1) within this study. Note that the wave height and wave period always remained the same in the four test series, i.e., H = 8.0 cm and T = 1.5 s.

3. Results and Discussion

3.1. Effect of Wave-Loading History on Wave-Induced Soil Responses

Both transient ($\widetilde{p}$) and residual pore pressure ($\overline{p}$) responses manifest as waves propagate over a silty bed. When residual liquefaction occurs, $\overline{p}$ reaches the initial overburden pressure (σ_0'), as expressed by

$$\overline{p} = \sigma_0' \tag{2}$$

where $\sigma_0' = \gamma' z$. Based on this liquefaction criterion, the observed maximum residual pore pressures ($\overline{p}_{\max}$) are compared with the calculated values of σ_0' to determine if liquefaction occurs at a specific depth within the soil. Given the non-uniform burial depths of the PPTs, explicit identification of the liquefaction depth proved challenging. For instance, in Test 1, the liquefaction criterion suggested an ultimate liquefaction depth (z_L) within the range of 17.5 cm < z_L < 27.5 cm. Moreover, the number of wave cycles required to induce liquefaction (N_l) at depths z = 2.5 cm, 7.5 cm, and 17.5 cm were determined as N_l = 102, 110, and 127, respectively (refer to Li et al. [25]). Despite only employing a constant wave period (i.e., T = 1.5 s) in the flume observations, one needs to be aware that the effect of the wave period on the evolution of the residual pore pressure may be significant. The pore pressure would build up more rapidly under small-period waves because the accumulated pore pressure is more difficult to dissipate within a short duration. Nevertheless, a higher ultimate level of residual pore pressure could be achieved in the case of large-period waves (i.e., long waves) because of the stronger wave energy contained in long waves [39]. As such, a seabed subjected to long waves is more prone to residual liquefaction.

It should be noted that the dissipation of accumulated excess pore pressure is associated with the consolidation process of the soil. Consequently, the silt bed experiences densification (or compaction), resulting in an increase in the void ratio (e) and relative density (D_r), as shown in Table 1. This wave-loading history further contributes to the noticeable settlement of the mudline. Table 2 summarizes the maximum liquefaction depth (z_L) and mudline settlement (s) after each test series. Notably, the settlement of the mudline diminishes with an increasing number of tests until no settlement is discernible in Test 4. The total mudline settlement approximates 3.5 cm, representing approximately 5.8% of the initial soil depths.

Table 2. The maximum liquefaction depths (z_L), maximum amplitude of interfacial waves (a_0), and mudline settlements (s) for four test series.

	Symbol	Test Series			
		Test 1 (D_r = 0.66)	**Test 2 (D_r = 0.71)**	**Test 3 (D_r = 0.76)**	**Test 4 (D_r = 0.78)**
Maximum liquefaction depth	z_L (cm)	17.5 < z_L < 27.5	15.8 < z_L < 25.8	4.7 < z_L < 14.7	0
Maximum amplitude of interfacial waves	a_0 (cm)	0.5	0.3	0.15	0
Settlement of the mudline	s (cm)	1.7	1.1	0.7	0

It is important to recognize the dynamic nature of the PPT burial depths, which varied due to mudline settlements. Throughout this study, the x-axis (i.e., z = 0) consistently denotes the location of the mudline in the current test series under the pre-test condition. This location gradually shifts downward post-mudline settlements. For example, in Test 1, PPT 1 is positioned at z = 2.5 cm, whereas in Test 2, it relocates to z = 0.8 cm (z = 2.5 cm–1.7 cm). In Tests 3 and 4, PPT 1 is no longer buried within the silt bed, i.e., it resides above the mudline ($z < 0$). Similarly, the liquefaction depth (z_L) is calculated relative to the mudline corresponding to the current test.

Upon the initiation of residual liquefaction, the silt undergoes a transition from a solid state to a viscous liquid state. This transformation results in the formation of a two-layered liquid system, comprising the upper pure-water region and the lower liquefied-soil region [24,29]. As a result, the incident surface waves induce oscillation in the mudline, generating a series of "interfacial waves" at the interface between the two liquid layers. During the residual liquefaction observed in the flume, the amplitude of the mudline oscillation, i.e., the amplitude of the interfacial waves, was recorded using a CCD camera. As the number of wave cycles (N) increased, the amplitude of the interfacial waves gradually expanded, reaching a maximum and maintaining that value until the cessation of wave loading. The maximum amplitude of the interfacial waves (a_0) for each of the four test series is listed in Table 2 for reference. The variations in the maximum liquefaction depth (z_L), maximum amplitude of interfacial waves (a_0), mudline settlement (s), and relative density (D_r) subjected to the four wave effects are also shown in Figure 3.

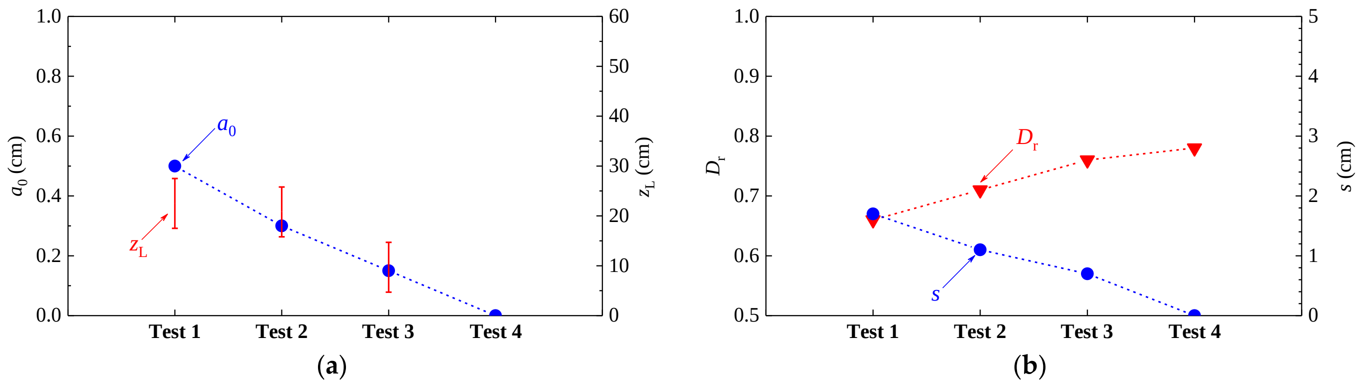

Figure 3. Effect of wave-loading history on the (**a**) maximum liquefaction depth (z_L) and maximum amplitude of interfacial waves (a_0); (**b**) settlement of the mudline (s) and relative density (D_r).

Figure 3 shows a decreasing trend in the liquefaction depth (z_L) with an increasing number of test series. In Test 4 (D_r = 0.78), where the silt bed did not liquefy, no interfacial waves were identified. This suggests that the resistance of the soil to residual liquefaction is enhanced when prior wave loadings have liquefied the silt bed. Correspondingly, the maximum amplitude of interfacial waves (a_0) decreases with the growth of the wave-loading history, aligning with the observation made by Sassa et al. [29] that the amplitude of the vertical displacement of the mudline increases with the depth of the liquefied soil.

In this section, the wave-induced pore pressure, considering the effect of the previous wave-loading history, is further examined. Figure 4 shows the total time series of the wave-induced pore pressure measured by PPT 2 for various test series. Here, N (= t/T) is the number of wave cycles, and p (=$\overline{p} + \widetilde{p}$) is the wave-induced excess pore pressure. To facilitate comparison with the wave height (H), the expression p/γ_w is used, where γ_w (=9.8 × 10^3 N/m^3) is the unit weight of water. Considering the mudline settlements (see Table 2 or Figure 3), the burial depths of PPT 2 in Tests 1~4 were 7.5 cm, 5.8 cm, 4.7 cm, and 4.0 cm, respectively. In accordance with the criterion for residual liquefaction (Equation (2)), the silt at the location of PPT 2 eventually liquefied in Tests 1~3, revealing three distinct stages in the liquefaction process (see Figure 4a–c). Despite the gradual shallowing of the burial depth of PPT 2, the corresponding number of wave cycles required to induce residual liquefaction (N_l) increased. The liquefaction was initiated at N_l = 110, 130, and 335 in Tests 1, 2, and 3, respectively. A similar observation of an increase in N_l with an increasing relative density (D_r) of the soil has been reported in undrained cyclic shear tests [40]. Moreover, the maximum residual pore pressure ($\overline{p}_{max}$) and the amplitude of the transient pore pressure ($|\widetilde{p}|$) in the continuous liquefaction stage were significantly reduced with an increasing number of tests. After the previous three liquefaction-densification cycles in Tests 1~3, the silt particles were densely contacted in Test 4 (D_r = 0.78). Consequently, only a slight accumulation of pore pressure was induced ($\overline{p}_{max}/\gamma_w = 1.44$ cm), and the transient pore pressure during wave loading was nearly negligible (see Figure 4d). Thus, the dense silt bed in Test 4 became resistant to liquefaction.

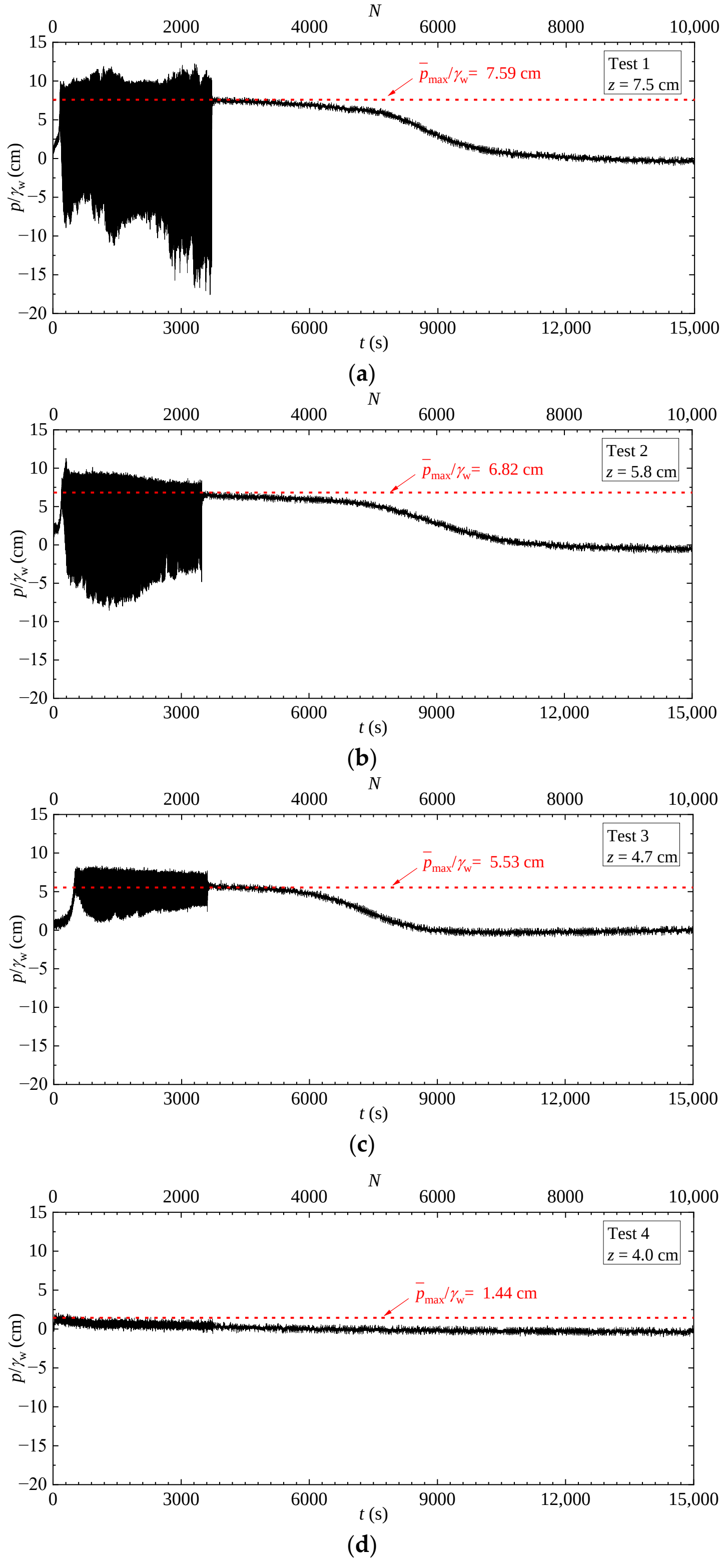

Figure 4. Total time series of the excess pore pressure measured by PPT 2 for various test series: (**a**) Test 1; (**b**) Test 2; (**c**) Test 3; and (**d**) Test 4.

To quantify the effect of the wave-loading history on the pore pressure buildup, Figure 5 shows the variations in the maximum residual pore pressure ratio ($\overline{p}_{\max}/\sigma_0'$) with the wave-loading history, as measured by PPTs 1~6. The non-dimensional pore pressure ratio ($\overline{p}_{\max}/\sigma_0'$) characterizes the maximum magnitude of pore pressure accumulation, where a smaller value indicates a stronger resistance of the soil to liquefaction [26]. Note that PPT 1 in Tests 3 and 4 was exposed to the pure-water layer due to mudline settlement; therefore, only data monitored by buried PPTs (i.e., $z > 0$) in a specific test series are considered. Liquefaction occurrences at certain burial depths of the PPTs are also marked in the figure. A decreasing trend in the values of $\overline{p}_{\max}/\sigma_0'$ is evident with an increasing wave-loading history, particularly during the transition of the silt bed from a liquefiable material to an un-liquefiable one (e.g., from Test 3 to Test 4 in the present physical modeling). With an increase in the number of tests, the submerged unit weight of soil (γ') would increase, while the burial depth (z) would decrease. Despite variations in γ' and z, the values of $\overline{p}_{\max}$ were approximately equal to the initial vertical effective stress ($\sigma_0' = \gamma' z$) (i.e., $\overline{p}_{\max}/\sigma_0' \approx 1$), as long as the occurrence of silt liquefaction could be monitored. In Test 4, only slight pore pressure accumulation was generated ($\overline{p}_{\max}/\sigma_0' < 0.4$), which proved insufficient to cause residual liquefaction. In conclusion, the repeated but intermittent wave loadings effectively mitigate the buildup of pore pressure, thereby enhancing the resistance of the soil to liquefaction. Additionally, the decreasing trends of $\overline{p}_{\max}/\sigma_0'$ the with wave-loading history, as measured by PPT 5 and PPT 6, were consistently observed. This indicates that the level of pore pressure accumulation scarcely varies with soil depth in the deep, un-liquefied soil layer.

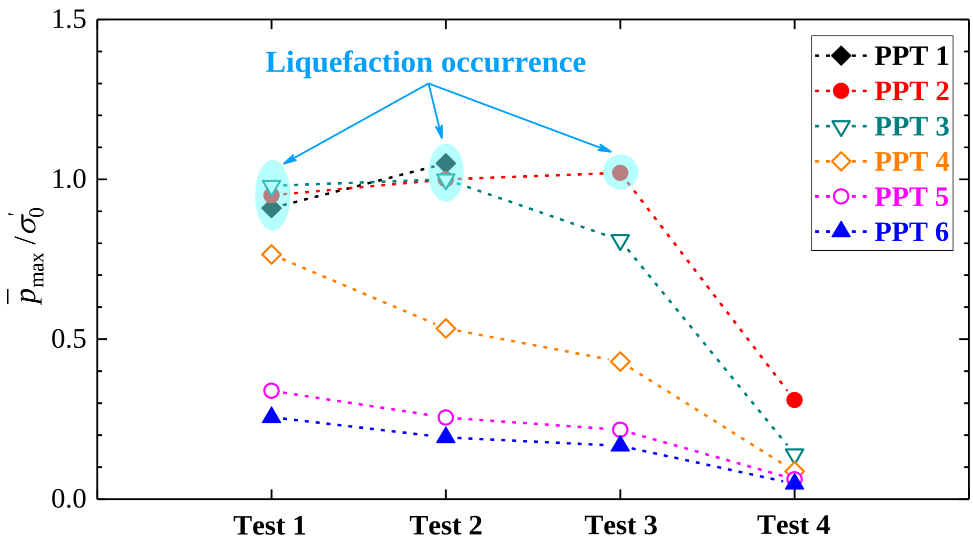

Figure 5. Variations in the maximum residual pore pressure ratio ($\overline{p}_{\max}/\sigma_0'$) with wave-loading history measured by PPTs 1~6.

In addition to residual pore pressure, the wave-induced transient pore pressure is also influenced by the wave-loading history. Upon the liquefaction of silt, the amplitude of the transient pore pressure experiences significant amplification, a phenomenon not observed in un-liquefied silt. Li et al. [25] introduced an amplification ratio (ζ) to quantify this amplification effect and distinguished the onset of residual liquefaction, which is defined as

$$\zeta = \frac{|\widetilde{p}|}{|\widetilde{p}|_{\mathrm{a}}} \tag{3}$$

where ζ is the amplification ratio, $|\widetilde{p}|$ is the measured amplitude of transient pore pressure at a specific soil depth, and $|\widetilde{p}|_{\mathrm{a}}$ is the corresponding amplitude of transient pore pressure predicted by Yamamoto et al. [15]. Essentially, ζ quantifies the relative magnitude of the actual pore pressure amplitude to the predicted pore pressure amplitude in the quasi-elastic stage. Figure 6a provides the detailed time series of the wave-induced pore pressure for $400 < N < 420$ measured by PPT 2 in Tests 1~4, and the variations in the amplification ratio of transient pore pressure (ζ) for $400 < N < 500$ with the wave-loading history measured by PPTs 1~6 are shown in Figure 6b. It should be noted that the wave duration $400 < N < 500$ falls within the continuous liquefaction stage if the soil at corresponding locations undergoes residual liquefaction. Liquefaction occurrences are also marked in the figure. As shown in Figure 6, the values of ζ exhibit a decreasing trend with an increasing number of tests in the shallow soil layer (e.g., PPTs 1~3), providing further evidence of the enhancement of the resistance of the soil to residual liquefaction. However, the values of ζ remain nearly constant and close to 1.0 for PPTs 4~6, suggesting that the effect of wave-loading history on the transient pore pressure is negligible in the relatively deep un-liquefied soil layer.

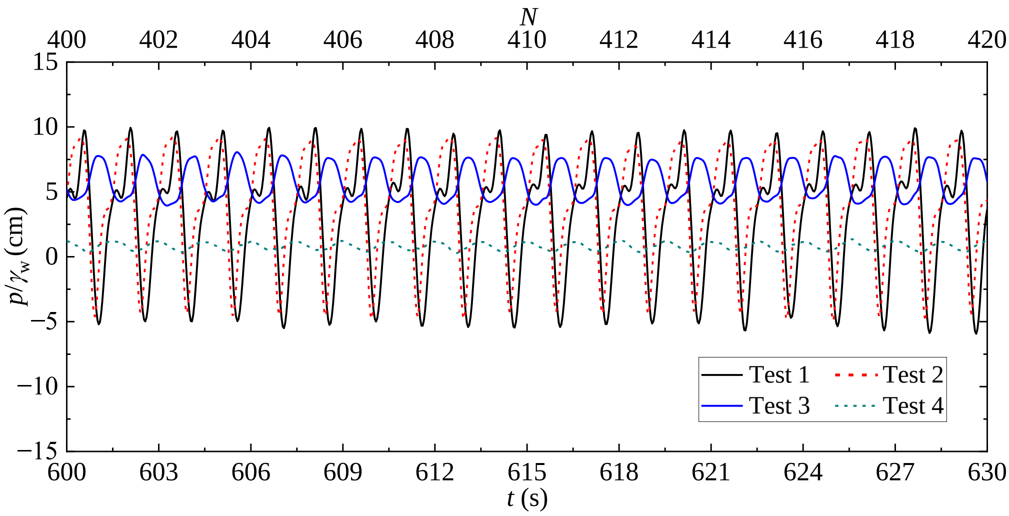

(**a**)

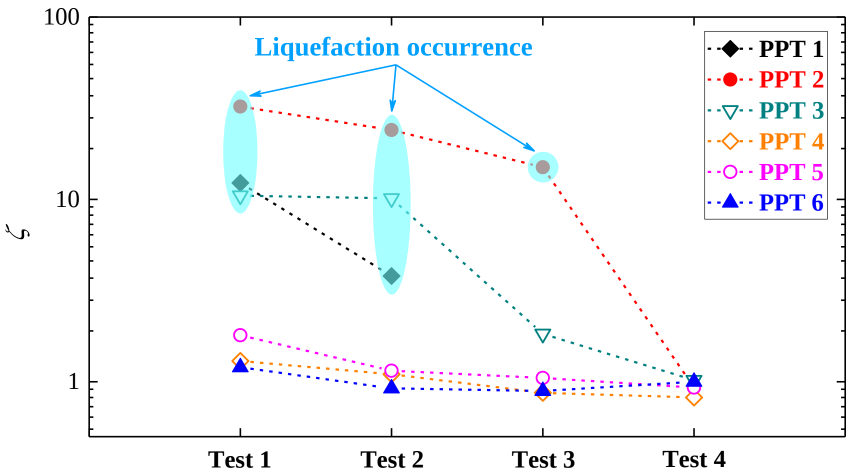

(**b**)

Figure 6. Effect of the wave-loading history on the transient pore pressure: (**a**) detailed time series of the wave-induced pore pressure for $400 < N < 420$ measured by PPT 2 for various test series; (**b**) variations in the amplification ratio of transient pore pressure (ζ) for $400 < N < 500$ with wave-loading history measured by PPTs 1~6.

3.2. Dissipation of Wave-Induced Pore Pressure

As previously mentioned, three distinct stages during residual liquefaction before the cessation of wave loading ($t < 3600$ s) have been identified. However, the pore pressure evolution in the post-liquefaction duration ($t > 3600$ s) was not thoroughly described.

Figure 7 shows the total time series of water surface elevation (η) and excess pore pressure (p/γ_w) at various soil depths in Test 1, where η is the water surface elevation measured with WG 3 (see Figure 7a). As depicted in Figure 7c–h, the residual pore pressure undergoes a notable dissipation process after the cessation of wave loading ($t > 3600$ s). The residual pore pressures ($\overline{p}_c$) at the moment of wave cessation ($t = 3600$ s) are also marked in Figure 7c–h for reference. Within the liquefied soil layer (i.e., $z \le 17.5$ cm; see Figure 7c~e), no apparent dissipation of pore pressure buildup is observed during wave loading ($0 < t < 3600$ s). Consequently, the residual pore pressure dissipates from its maximum value ($\overline{p}_{max}$) to zero after wave loading ceases ($t > 3600$ s), i.e., $\overline{p}_c = \overline{p}_{max}$. Following wave cessation, the residual pore pressures for $z \le z_L$ also remain near their maximum value for some time (e.g., 3600 s $< t <$ 4500 s; see Figure 7c–e). Similar features of pore pressure dissipation for liquefiable sand beds in a centrifuge were reported by Sassa and Sekiguchi [26]. In contrast, within the un-liquefied layer ($z > 17.5$ cm; see Figure 7f–h), the accumulated pore pressure begins to slightly dissipate after reaching its maximum value ($\overline{p}_{max}$) for $t < 3600$ s, i.e., $\overline{p}_c < \overline{p}_{max}$. Moreover, the dissipation of excess pore pressure is significantly accelerated after wave loading ceases ($t > 3600$ s) for $z > 17.5$ cm.

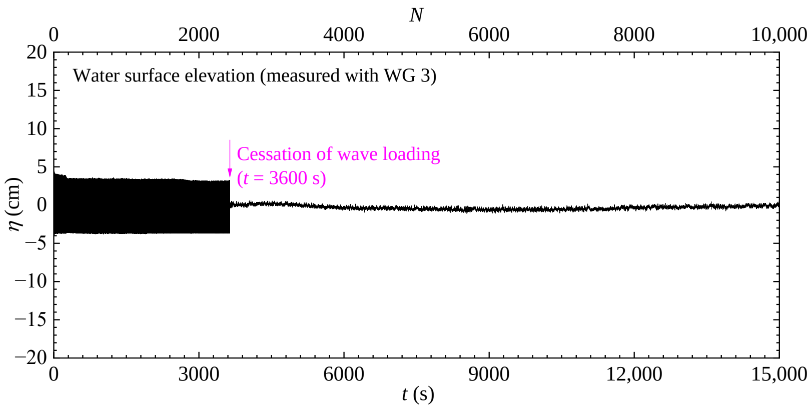

(**a**)

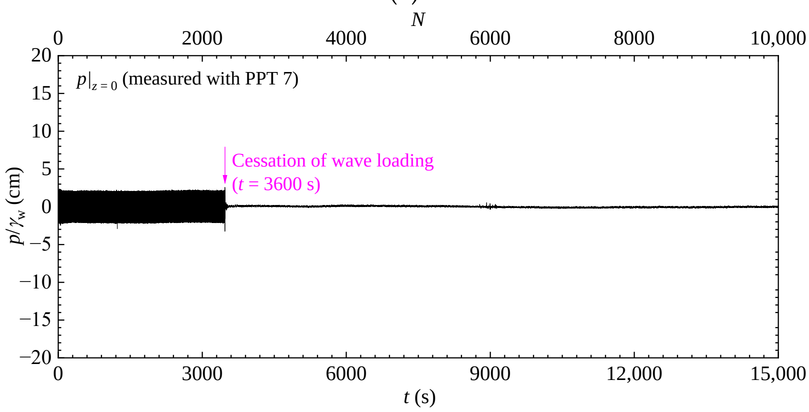

(**b**)

Figure 7. *Cont.*

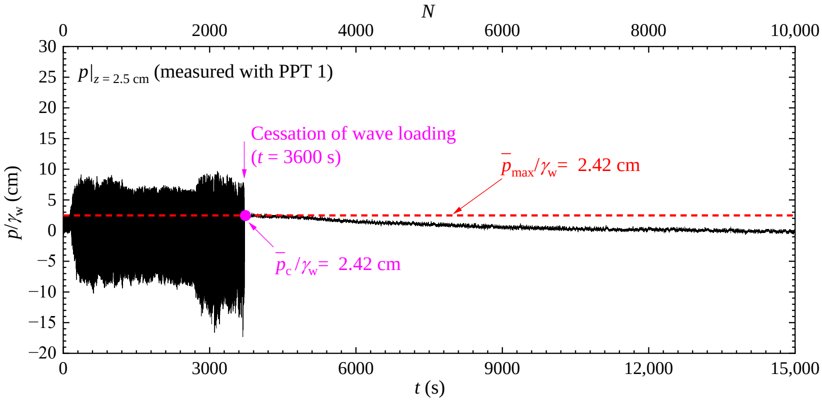

(**c**)

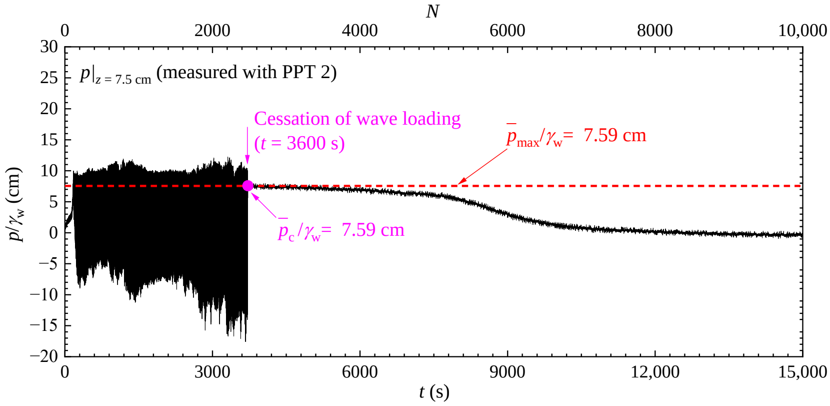

(**d**)

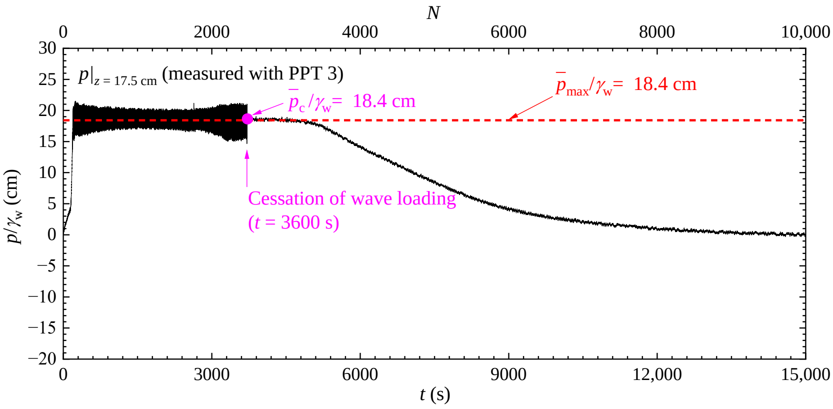

(**e**)

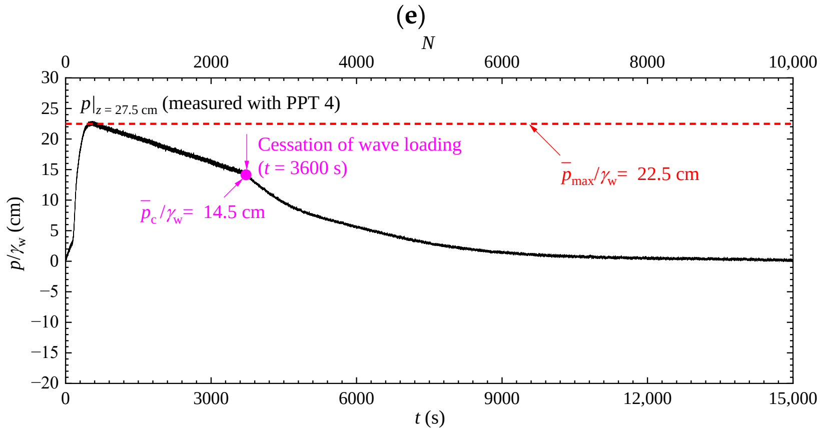

(**f**)

Figure 7. *Cont.*

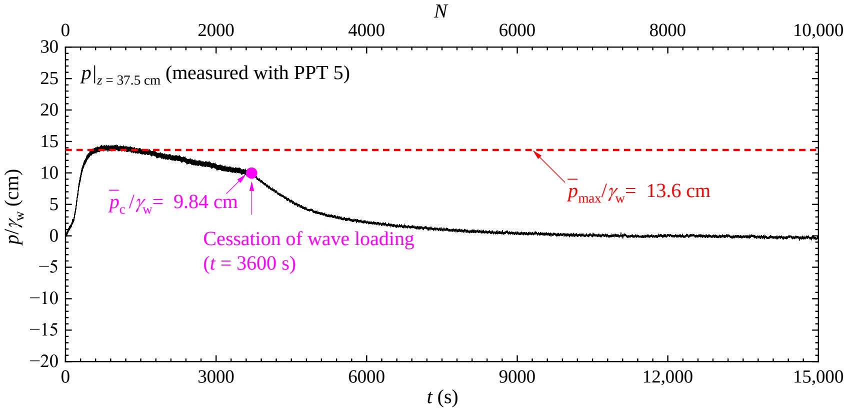

(g)

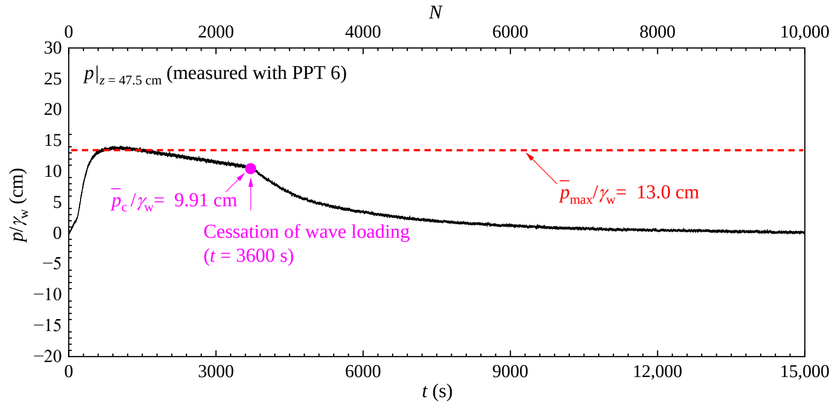

(h)

Figure 7. Total time series of the water surface elevation (η) and the excess pore pressure (p/γ_w) at various soil depths in Test 1: (**a**) η; (**b**) z = 0 (mudline); (**c**) z = 2.5 cm; (**d**) z = 7.5 cm; (**e**) z = 17.5 cm; (**f**) z = 27.5 cm; (**g**) z = 37.5 cm; and (**h**) z = 47.5 cm.

To illustrate the dissipation nature of excess pore pressure, Figure 8 shows the vertical distribution of $\overline{p}_{max}$ and $\overline{p}_c$. Within the liquefied soil zone ($z \leq 17.5$ cm), the maximum residual pore pressure is identical to the overburden effective stress, i.e., $\overline{p}_{max} = \gamma' z$, as mentioned in Section 3.1. Although an upward-directed pressure gradient is generated, the residual pore pressure is maintained at its maximum value ($\overline{p}_c = \overline{p}_{max}$), even after the wave ceases (e.g., 3600 s < t < 4500 s). As such, the process of residual liquefaction slows down the dissipation of excess pore pressure. This implies that the liquefied silt may be undrained before a reduction in residual pore pressure is discernible (t > 4500 s). However, it should be noted that pore pressure dissipation cannot be indefinitely withheld; the pore pressure in the liquefied silt layer eventually dissipates if the duration of wave loading is sufficiently long [10]. Within the un-liquefied soil zone (z > 17.5 cm), it is evident that $\overline{p}_c < \overline{p}_{max} < \gamma' z$. This evolution of excess pore pressure indicates that the un-liquefied silt bed behaves as a partially drained medium, wherein pore pressure accumulation coexists with its dissipation. Before the residual pore pressure reaches its maximum value (e.g., t < 400 s for z = 27.5 cm; see Figure 7f), the accumulation mechanism, primarily attributed to the shear contraction tendency of soil under cyclic wave actions, dominates the evolution of pore pressure. Subsequently (400 s < t < 3600 s; see Figure 7f), the residual pore pressure is reduced from $\overline{p}_{max}$ to $\overline{p}_c$, indicating that the dissipation mechanism surpasses the accumulation mechanism. As the wave loading ceases (t > 3600 s; see Figure 7f), the accumulation mechanism vanishes, causing the pore pressure to exhibit accelerated dissipation.

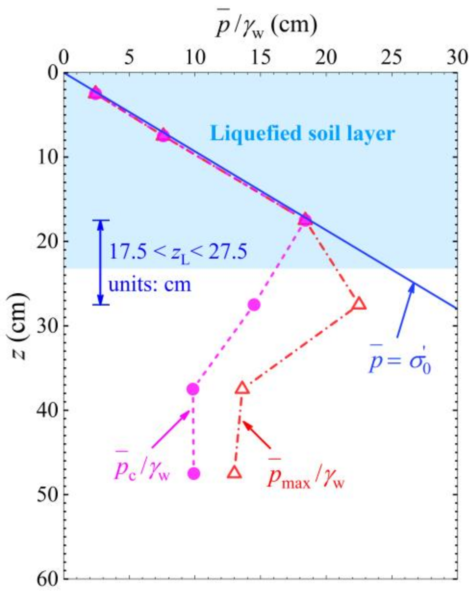

Figure 8. Vertical distribution of the maximum residual pore pressure ($\overline{p}_{max}$) and the residual pore pressure at the moment of wave cessation ($\overline{p}_c$).

3.3. Reshaping of the Silt Bed Topography

Due to the liquefaction–densification cycle, the topography of a silt bed undergoes significant reshaping. Sumer et al. [24] reported that ripples begin to emerge on the bed when the compaction process is completed. As the waves continue, these initial bed ripples grow in size and eventually attain an equilibrium state. Yang et al. [41] observed the formation of small hilly deposits on the surface of a silt bed after wave action ceased. However, their investigations did not delve into the effect of the wave-loading history on the formation of the bed topography. To address this limitation, Figure 9 presents typical snapshots of the bed topography after the pore pressure dissipation process across various test series. The formation of the bed topography is notably related to the wave-loading history. In Tests 1 and 2, numerous mud volcanoes were observed on the surface of the silt bed, as shown in Figure 9a,b. These volcano structures bear a resemblance to the sand boils observed after earthquakes at sites where sand deposits have liquefied. In contrast, Test 3 and Test 4 displayed the formation of ripples, which appeared before the wave-loading ceased (see Figure 9c,d). It was also observed that under the wave action, the preceding topography of the silt bed was erased upon soil liquefaction, and the fresh one was gradually formed thereafter.

Expanding on these findings, the volcano-shaped structures in Test 1 and Test 2 were upward seepage channels caused by the drainage process. The fine particles in the lower part of the silt bed may rapidly move up along these small seepage channels [41]. Side views of these structures, exhibiting various geometrical scales, can be observed in Figure 10. Notably, these mud volcanoes had diameters and heights of no more than 5.0 cm and 2.0 cm, respectively. Additionally, a higher distribution density of mud volcanoes can be observed in Test 1 (see Figure 9a) compared with that in Test 2 (see Figure 9b). However, in cases of mild liquefaction (as in Test 3; see Figure 9c) or no liquefaction (as in Test 4; see Figure 9d), these mud volcanoes were absent, replaced by wave-induced ripples on the bed surface. Therefore, the topography of the silt bed can serve as a clear indicator of prior liquefaction events, transforming from mud volcanoes to ripples as the liquefaction depth decreases.

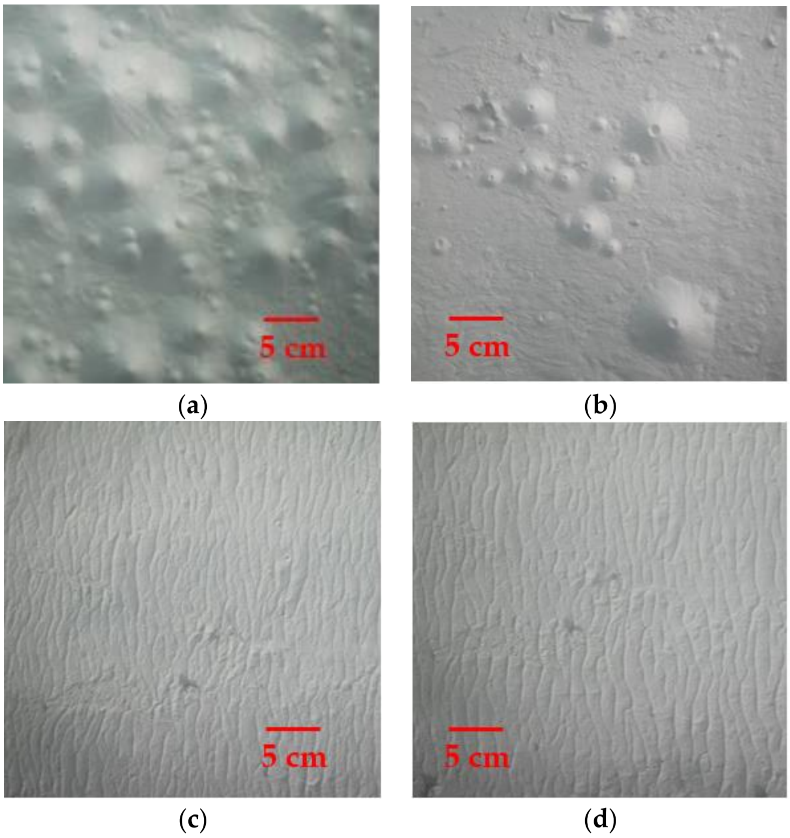

Figure 9. Snapshots of the typical topography of the silt bed after pore pressure dissipation for various test series (top view): (**a**) Test 1; (**b**) Test 2; (**c**) Test 3; and (**d**) Test 4.

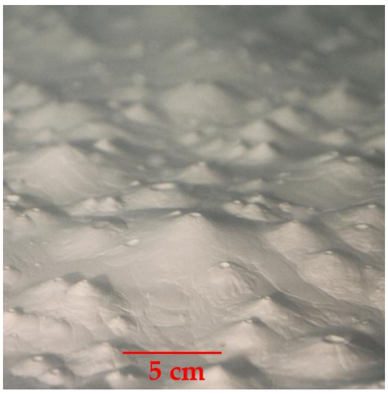

Figure 10. Snapshot of the volcano-shaped topography for the post-liquefied silt bed.

Considering the significant effect of the wave-loading history on the sequential evolution of residual liquefaction in a silty seabed, an important concern in the practice of ocean engineering would be determining the critical relative density for the onset of liquefaction. Given the severity of progressive wave loading acting on a seabed, which may be characterized by the cyclic stress ratio [25,26], such a threshold of silt density needs to be further established.

If the target seabed is prone to liquefaction in the design of offshore structures, interventions that would prevent this liquefaction should be carefully considered. Generally, there are two basic preventive strategies. The first one is to improve the soil properties. Such interventions include the use of appropriate backfill (e.g., densely-packed sand) and surface protection by cover stones or filter stones. The second strategy is to drain out the excess pore pressure or prevent the pore pressure from accumulating. For instance, drainage pads and wells can be installed near the foundation of marine structures. More detailed countermeasures against soil liquefaction can be found in [10].

4. Conclusions

This study investigated the effect of the wave-loading history on the evolution of residual liquefaction in a silty seabed through a series of wave flume tests. The following conclusions are drawn based on flume observations:

(1) A previous wave-loading history densifies the silt bed, causing a noticeable settlement of the mudline. With increasing wave-loading exposure, the ultimate liquefaction depth (z_L), the maximum amplitude of interfacial waves (a_0), and the mudline settlement (s) are reduced during each wave sequence. The maximum residual pore pressure ratio ($\overline{p}_{max}/\sigma_0'$) exhibits a declining trend, and the number of wave cycles required to induce liquefaction (N_l) increases. The accumulation of pore pressure significantly diminishes when the silt bed resists liquefaction. Furthermore, the amplification ratio of transient pore pressure (ζ) in the shallow liquefied soil layer decreases with an increasing number of tests. Essentially, the liquefaction resistance of the soil is enhanced by the preceding wave-loading history.

(2) Within the liquefied soil layer, residual pore pressure is maintained at its peak during the continuous liquefaction stage. Conversely, in non-liquefied regions, the pore pressure exhibits a slight dissipation after reaching its peak during the wave activity. Furthermore, the dissipation of residual pore pressure accelerates after the cessation of wave loading.

(3) Due to the liquefaction–densification cycles, the topography of the silt bed can be reshaped. Severe liquefaction prompts the formation of volcano-shaped seepage channels on the surface of the silt, while in the case of mild liquefaction or no liquefaction, mud volcanoes are absent and replaced by ripples on the bed surface. Therefore, the topography of the silt bed may serve as an indicator of prior liquefaction events.

Author Contributions: Conceptualization, F.G. and Y.W.; experiments and data analyses, C.L. and J.Y.; writing—original draft, C.L.; validation, Y.W. and W.Q.; review and editing, F.G., Y.W., W.Q., J.Y. and C.L. All authors have read and agreed to the published version of the manuscript.

Funding: This work was funded by the National Natural Science Foundation of China (grant nos. 12061160463 and 11825205).

Institutional Review Board Statement: Not applicable.

Informed Consent Statement: Not applicable.

Data Availability Statement: The data presented in this study are available upon request from the corresponding author.

Conflicts of Interest: The authors declare no conflicts of interest.

Notations

a_0	Maximum amplitude of the interfacial waves
c	Cohesion of the soil
d	Water depth
d_{10}	Effective grain size
d_{50}	Mean grain size
D_r	Relative density
e	Void ratio
e_{max}	Maximum void ratio
e_{min}	Minimum void ratio
g	Gravitational acceleration
G_s	Specific weight of the soil

H	Wave height
I_p	Plasticity index
k_s	Coefficient of permeability
L	Wave length
N	Number of wave cycles
N_l	Number of wave cycles to cause liquefaction
p	Wave-induced pore pressure within the soil
$\overline{p}$	Residual pore pressure
$\overline{p}_{\max}$	Maximum residual pore pressure
$\overline{p}_c$	Residual pore pressure on the occasion of wave cessation
$\widetilde{p}$	Transient pore pressure
s	Settlement of the mudline
T	Wave period
t	Time
w	Water content of the soil
z	Soil depth calculated from the mudline
z_L	Maximum liquefaction depth
η	Wave surface elevation
φ	Angle of friction
γ'	Buoyant unit weight of soil
γ_w	Unit weight of water
σ'_0	Initial overburden effective stress
$\lvert\widetilde{p}\rvert$	Amplitude of the transient pore pressure
$\lvert\widetilde{p}\rvert_a$	Pore pressure amplitude predicted by Yamamoto et al. [15]
ζ	Amplification ratio

References

1. Bea, R.G.; Wright, S.G.; Sircar, P.; Niedoroda, A.W. Wave-induced slides in south pass block 70, Mississippi delta. *J. Geotech. Eng.* **1983**, *109*, 619–644. [CrossRef]
2. Sumer, B.M.; Fredsøe, J.; Christensen, S.; Lind, M.T. Sinking/floatation of pipelines and other objects in liquefied soil under waves. *Coast. Eng.* **1999**, *38*, 53–90. [CrossRef]
3. Teh, T.C.; Palmer, A.; Damgaard, J. Experimental study of marine pipelines on unstable and liquefied seabed. *Coast. Eng.* **2003**, *50*, 1–17. [CrossRef]
4. de Groot, M.B.; Kudella, M.; Meijers, P.; Oumeraci, H. Liquefaction phenomena underneath marine gravity structures subjected to wave loading. *J. Waterw. Port Coast. Ocean Eng.* **2006**, *132*, 325–335. [CrossRef]
5. Li, X.J.; Gao, F.P.; Yang, B.; Zang, J. Wave-induced pore pressure responses and soil liquefaction around pile foundation. *Int. J. Offshore Polar Eng.* **2011**, *21*, 233–239.
6. Gao, F.P.; Li, J.H.; Qi, W.G.; Hu, C. On the instability of offshore foundations: Theory and mechanism. *Sci. China Phys. Mech. Astron.* **2015**, *58*, 124701. [CrossRef]
7. Qi, W.G.; Shi, Y.M.; Gao, F.P. Uplift soil resistance to a shallowly-buried pipeline in the sandy seabed under waves: Poro-elastoplastic modeling. *Appl. Ocean. Res.* **2020**, *95*, 102024. [CrossRef]
8. Zen, K.; Yamazaki, H. Mechanism of wave-induced liquefaction and densification in seabed. *Soils Found.* **1990**, *30*, 90–104. [CrossRef] [PubMed]
9. Sumer, B.M.; Fredsøe, J. *The Mechanics of Scour in the Marine Environment*; World Scientific: Singapore, 2002.
10. Sumer, B.M. *Liquefaction Around Marine Structures*; World Scientific Publishing Co.: Singapore, 2014.
11. Jeng, D.S. *Mechanics of Wave-Seabed-Structure Interactions: Modelling, Processes and Applications*; Cambridge University Press: Cambridge, UK, 2018.
12. Putnam, J.A. Loss of wave energy due to percolation in a permeable sea bottom. *Eos Trans. Am. Geophys. Union* **1949**, *30*, 349–356.
13. Reid, R.O.; Kajirua, K. On the damping of gravity waves over a permeable seabed. *Eos Trans. Am. Geophys. Union* **1957**, *38*, 662–666.
14. Moshagen, H.; Tørum, A. Wave induced pressures in permeable seabeds. *J. Waterw. Harbors Coastal Eng. Div. Am. Soc. Civ. Eng.* **1975**, *101*, 49–57. [CrossRef]
15. Yamamoto, T.; Koning, H.L.; Sellmeijer, H.; Hijum, E.V. On the response of a poro-elastic bed to water waves. *J. Fluid Mech.* **1978**, *87*, 193–206. [CrossRef]
16. Madsen, O.S. Wave-induced pore pressures and effective stresses in a porous bed. *Géotechnique* **1978**, *28*, 377–393. [CrossRef]
17. Mei, C.C.; Foda, M.A. Wave-induced responses in a fluid-filled poro-elastic solid with a free surface—A boundary layer theory. *Geophys. J. R. Astr. Soc.* **1981**, *66*, 597–631. [CrossRef]
18. Hsu, J.R.C.; Jeng, D.S. Wave-induced soil response in an unsaturated anisotropic seabed of finite thickness. *Int. J. Numer. Anal. Methods Geomech.* **1994**, *18*, 785–807. [CrossRef]

19. Bear, J. *Dynamics of Fluids in Porous Media*; Courier Dover Publications: Dove, DE, USA, 1972.
20. Qi, W.G.; Gao, F.P. Wave induced instantaneously-liquefied soil depth in a non-cohesive Seabed. *Ocean Eng.* **2018**, *153*, 412–423. [CrossRef]
21. Zhou, M.Z.; Qi, W.G.; Jeng, D.S.; Gao, F.P. A non-Darcy flow model for a non-cohesive seabed involving wave-induced instantaneous liquefaction. *Ocean Eng.* **2021**, *239*, 109807. [CrossRef]
22. Seed, H.B.; Rahman, M.S. Wave-induced pore pressure in relation to ocean floor stability of cohesionless soils. *Mar. Georesour. Geotechnol.* **1978**, *3*, 123–150. [CrossRef]
23. Foda, M.A.; Tzang, S.Y. Resonant fluidization of silty soil by water waves. *J. Geophys. Res.* **1994**, *99*, 20463–20475. [CrossRef]
24. Sumer, B.M.; Hatipoglu, F.; Fredsøe, J.; Sumer, S.K. The sequence of sediment behavior during wave-induced liquefaction. *Sedimentology* **2006**, *53*, 611–629. [CrossRef]
25. Li, C.F.; Wang, Y.; Gao, F.P.; Yang, L.J. Spatiotemporal evolution of excess pore pressures in a silty seabed under progressive waves during residual liquefaction. *Appl. Ocean Res.* **2022**, *129*, 103401. [CrossRef]
26. Sassa, S.; Sekiguchi, H. Wave-induced liquefaction of beds of sand in a centrifuge. *Géotechnique* **1999**, *49*, 621–638. [CrossRef]
27. Miyamoto, J.; Sassa, S.; Sekiguchi, H. Progressive solidification of a liquefied sand layer during continued wave loading. *Géotechnique* **2004**, *54*, 617–629. [CrossRef]
28. Rahman, M.S.; Jaber, W.Y. A simplified drained analysis for wave-induced liquefaction in ocean floor sands. *Soils Found.* **1986**, *26*, 57–68. [CrossRef]
29. Sassa, S.; Sekiguchi, H.; Miyamoto, J. Analysis of progressive liquefaction as a moving-boundary problem. *Géotechnique* **2001**, *51*, 847–857. [CrossRef]
30. Jeng, D.S.; Seymour, B.; Gao, F.P.; Wu, Y.X. Ocean waves propagating over a porous seabed: Residual and oscillatory mechanisms. *Sci. China Ser. E Technol. Sci.* **2007**, *50*, 81–89. [CrossRef]
31. Jeng, D.S.; Seymour, B.R. Simplified analytical approximation for pore-water pressure buildup in marine sediments. *J. Waterw. Port Coast. Ocean Eng.* **2007**, *133*, 309–312. [CrossRef]
32. Cheng, L.; Sumer, B.M.; Fredsøe, J. Solutions of pore pressure build up due to progressive waves. *Int. J. Numer. Anal. Methods Geomech.* **2001**, *25*, 885–907. [CrossRef]
33. Liu, X.L.; Cui, H.N.; Jeng, D.S.; Zhao, H.Y. A coupled mathematical model for accumulation of wave-induced pore water pressure and its application. *Coast. Eng.* **2019**, *154*, 103577. [CrossRef]
34. Duan, L.; Wang, D. Novel three-dimensional numerical model for residual seabed response to natural loadings near a single pile. *Appl. Ocean Res.* **2020**, *94*, 102004. [CrossRef]
35. Ülker, M.B.C. A combined theoretical and numerical modeling study of cyclic nonlinear response of sandy seabed. *Ocean Eng.* **2021**, *219*, 108348. [CrossRef]
36. Sui, T.; Sumer, B.M.; Kirca, V.S.O.; Carstensen, S.; Zheng, J.; Fuhrman, D.R. Effect of history of wave exposure on seabed liquefaction. *Coast. Eng.* **2023**, *183*, 104307. [CrossRef]
37. Chapuis, R.P. Predicting the saturated hydraulic conductivity of sand and gravel using effective diameter and void ratio. *Can. Geotech. J.* **2004**, *41*, 787–795. [CrossRef]
38. Boulanger, R.W.; Idriss, I.M. Liquefaction susceptibility criteria for silts and clays. *J. Geotech. Geoenviron. Eng.* **2006**, *132*, 1413–1426. [CrossRef]
39. Jeng, D.S.; Seymour, B.R.; Li, J. A new approximation for pore pressure accumulation in marine sediment due to water waves. *Int. J. Numer. Anal. Meth. Geomech.* **2007**, *31*, 53–69. [CrossRef]
40. de Groot, M.B.; Bolton, M.D.; Foray, P.; Meijers, P.; Palmer, A.C.; Sandven, R.; Sawicki, A.; The, T.C. Physics of liquefaction phenomena around marine structures. *J. Waterw. Port Coast. Ocean Eng.* **2006**, *132*, 227–243. [CrossRef]
41. Yang, Z.; Zhu, Y.; Liu, T.; Sun, Z.; Ling, X.; Yang, J. Pumping effect of wave-induced pore pressure on the development of fluid mud layer. *Ocean Eng.* **2019**, *189*, 106391. [CrossRef]